Pardini, F., Quessier, M., Naismith, A., Watson, M., Clarisse, L., & Burton, M. (2019). Initial constraints on triggering mechanisms of the eruption of Fuego volcano (Guatemala) from 3 June 2018 using IASI satellite data. *Journal of Volcanology and Geothermal Research*, *376*, 54-61. https://doi.org/10.1016/j.jvolgeores.2019.03.014

Journal of Volcanology and Geothermal Research 376 (2019) 54–61

Contents lists available at ScienceDirect

Journal of Volcanology and Geothermal Research

journal homepage: www.elsevier.com/locate/jvolgeores

Short communication

Initial constraints on triggering mechanisms of the eruption of Fuego volcano (Guatemala) from 3 June 2018 using IASI satellite data

F. Pardini [a], M. Queißer [a,*], A. Naismith [b], I.M. Watson [b], L. Clarisse [c], M.R. Burton [a]

[a] School of Earth and Environmental Sciences, University of Manchester, Oxford Road, Manchester M13 9PL, England, UK
[b] School of Earth Science, University of Bristol, Wills Memorial Building, Queens Road, Bristol BS8 1RJ, UK
[c] Université Libre de Bruxelles (ULB), Atmospheric Spectroscopy, Service de Chimie Quantique et Photophysique, Brussels, Belgium

ARTICLE INFO

Article history:
Received 1 October 2018
Received in revised form 14 March 2019
Accepted 22 March 2019
Available online 24 March 2019

Keywords:
IASI
SO_2
3 June 2018
Fuego
Eruption
Paroxysmal

ABSTRACT

On 3 June 2018 Volcán de Fuego (Guatemala) erupted explosively with unusual intensity, producing wide-spread ash dispersal and pyroclastic flows of >11 km length, which destroyed a community on Fuego's flanks, causing hundreds of fatalities. Here, we analyze satellite measurements of the SO_2 plume emitted during the most intense eruptive phase. Key eruption parameters including the injection height and SO_2 flux time-series indicate a degassing intensity at least three orders of magnitude above baseline levels. Our results suggest a steady ~2.5 hour climactic paroxysmal phase of the eruption with a mass eruption rate of ~1.4kg s^{-1} based on the combination of plume height estimates and an eruption column model, producing 0.03 ± 0.004 km^3 of tephra. We detect at least 130 kt of emitted SO_2 from satellite images, producing a minimum dissolved magmatic sulfur concentration of 500 ppm. Possible source mechanisms are discussed, which may be useful in assessing the risks posed by future large-magnitude eruptions to the large populations that live on Fuego's flanks. This study shows that even under challenging conditions of a tropical atmosphere during the rainy season, vital eruption parameters to constrain source mechanisms of eruptions can be retrieved from satellite remote sensing data.

1. Introduction

On 3 June 2018 at noon UTC, the Guatemalan scientific monitoring agency Instituto Nacional de Sismología, Vulcanología, Meteorología e Hidrología (INSIVUMEH) reported in a special bulletin the beginning of an eruption at Volcán de Fuego (Fuego volcano, Guatemala). At 17:30 UTC the eruption intensified, with ash plumes rising to at least 9km a.s.l (Global Volcanism Program, 2018a). A series of large pyroclastic flows were generated, traveling >11 km down Barranca Las Lajas and destroying the Las Lajas bridge on National Route (RN) 14 and the community of San Miguel Los Lotes. Official figures state hundreds of fatalities (at least 190) and people missing, while thousands of people were evacuated (Global Volcanism Program, 2018a, b; CONRED, 2018). According to VAAC bulletins and satellite observations, the most intense phase of the eruption took place between 17:30 and 20:00 UTC on 3 June 2018.

The 3763 m high Fuego volcano is located at 14.47°N, 90.88°W (Fig. 1), part of the Central American Volcanic Arc (Chesner and Rose, 1984) and classified as a basaltic to basaltic-andesitic arc volcano (Rose et al., 1978; Sisson and Layne, 1993; Lyons et al., 2010). Fuego has produced at least 50 significant eruptions in the last 500 years (Davies et al., 1978), but its activity is dominated by persistent Strombolian activity with eruption of mafic lava (Chesner and Rose, 1984). Compared with all other Fuego eruptions, the 3 June 2018 eruption of Fuego is unprecedented within the 20th – 21st centuries in terms of the number of human casualties it caused (Witham, 2005), and within the current (1999–present) eruptive regime for the intensity of the eruption (Naismith et al., 2019). Gaining insight into the mechanisms that produced this eruption is of importance to contextualize the eruptive event within the longer life cycle of Fuego's behavior, and to aid understanding of its behavior in the near future.

To that end satellite remote sensing is a very valuable technique as it provides regular monitoring data from a safe distance. This makes it suitable to eliminate biases caused by observational gaps in space and time, which is of great importance in volcanology. Satellite monitoring of volcanoes has proven to be beneficial both for monitoring and for concerns of public safety including decision-making processes, especially for volcanoes challenging to reach or poorly monitored. This can clearly be seen in recent applications of satellite remote sensing to monitoring Fuego itself (Webley et al., 2008; Lyons et al., 2010). As a magmatic gas that is directly linked to processes in the magmatic plumbing system, which is furthermore relatively easy to resolve from space, SO_2 is of high informational value for remote volcano monitoring (Carn et al., 2016). Indeed, ultraviolet (UV) and infrared (IR) sensors onboard satellite platforms are currently employed for the daily detection

* Corresponding author.
E-mail address: manuelqueisser@web.de (M. Queißer).

https://doi.org/10.1016/j.jvolgeores.2019.03.014

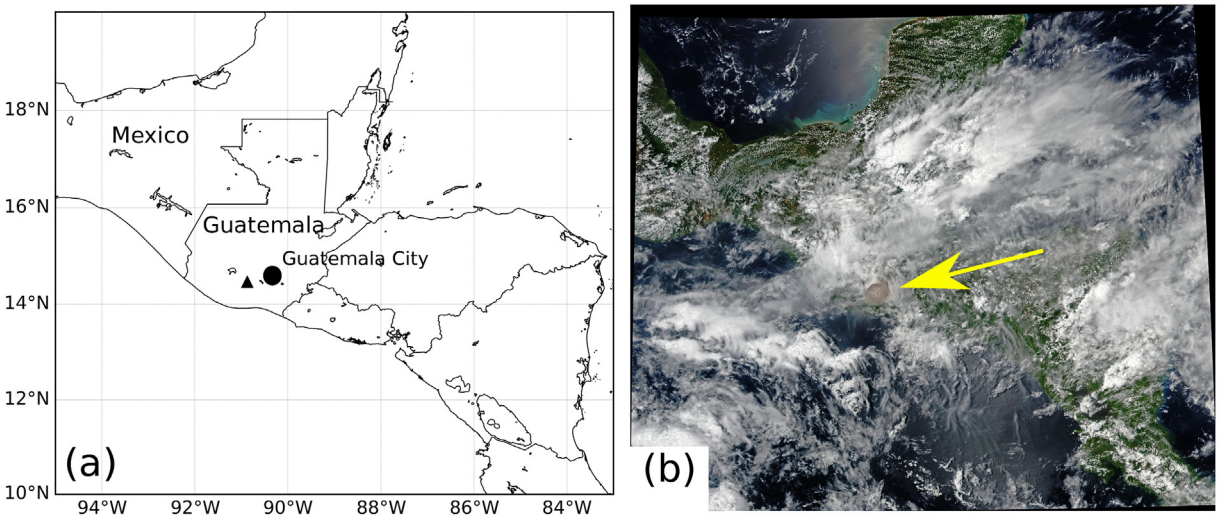

Fig. 1. Situation of the eruption. (a) Geographic location of Fuego volcano (triangle) in Guatemala. (b) Image of the eruption as seen by the Visible Infrared Imaging Radiometer Suite (VIIRS) on Suomi NPP at 19:00 UTC on 3 June 2018 (modified from https://disasters.nasa.gov/mount-fuego-eruption-2018). The ash plume, marked by the arrow, is clearly visible.

of volcanic SO_2 emissions. SO_2 can be measured in the UV spectra by OMI (Ozone Monitoring Instrument), GOME-2 (Global Ozone Monitoring Experiment–2) and OMPS (Ozone Mapping and Profile Suite), while measurements in the IR bands are done by MODIS (Moderate Resolution Imaging Spectroradiometer), AIRS (Atmospheric Infrared Sounder), IASI (The Infrared Atmospheric Sounding Interferometer), VIIRS (Visible Infrared Imaging Radiometer Suite) and CrIS (Cross-track Infrared Sounder). Together they can provide up to 18 daily SO_2 acquisitions.

In this work, measurements from IASI are used to retrieve SO_2 flux and injection height time-series during the most intense phase of the Fuego eruption. Plume height above the vent is then used as input to invert for mass eruption rate (*MER*), which, together with the atmospheric SO_2 loading, allows inferring the amount of magmatic sulfur (S) dissolved in the melt driving the eruption. The latter is a key piece of information to constrain the triggering mechanisms of the eruption. Based on this initial evidence and on previous observations and analysis of eruptive activity at Fuego volcano, an initial source mechanism for the recent eruption is discussed. Petrological analysis of eruption products is needed to arrive at a definite initial S content. However, this work demonstrates that satellite remote sensing data combined with eruption column models provide an additional independent constraint, with the advantage of quantifying the total S content present during the eruption process (e.g. Pardini et al., 2018).

2. Materials and methods

Quantifying SO_2 mass emission rates (flux) during continuous and eruptive degassing alike may provide crucial insights into volcanic processes, support volcanic hazard mitigation plans and help in quantifying the impact of volcanic eruptions on the environment and climate (e.g., Heard et al., 2012; Flemming and Inness, 2013; Sears et al., 2013; Theys et al., 2013). Satellite imagery of volcanic SO_2 plumes provides vertical columns (VCs), which are a valuable resource to that end. The retrieval of SO_2 vertical columns from UV and IR satellite measurements is done through algorithms optimised for the different sensors and quantification challenges, including the requirement to detect passive degassing at low heights or in explosive eruptions with large SO_2 yields. To perform accurate SO_2 retrievals, these algorithms require an a-priori estimate of the altitude at which SO_2 is located. To solve for SO_2 plume height, dedicated satellite retrievals both in the UV (Rix et al., 2012; Efremenko et al., 2017) and IR (Clarisse et al., 2014; Carboni et al., 2016) have been developed. With these algorithms, both plume height and SO_2 VCs can be computed. However, plume height is usually not available in real time and SO_2 VCs are computed for a set of assumed plume altitudes.

For the present study we used satellite observations acquired by IASI. There are currently two IASI instruments in operation: one on MetOp-A satellite and another on MetOP-B. Both operate in tandem on a polar orbit with a spatial resolution of ~12×12 km^2, providing global observations twice a day. We used observations acquired by MetOp-A and MetOp-B on 4 June 2018 at about 03:00 UTC (21:30 local time on 3 June 2018), hence about 9 h after the eruption had begun its climactic paroxysmal phase. The SO_2 vertical columns used here have been produced by applying the retrieval algorithm presented in Clarisse et al. (2012). The data product contains seven images with VCs corresponding to the following plume heights (asl): 5 km, 7 km, 10 km, 13 km, 16 km, 19 km and 25 km (see Supplementary materials, Text S1). Fig. 2 shows the VCs for the 19 km level, which approximately represents the altitude of the plume. If an assessment of plume height is available (e.g., through independent observations and/or measurements), VCs can be corrected for plume height by interpolating the set of VCs at the assessed plume altitude. To that end, numerical models applied to SO_2 images (Hughes et al., 2012; Heng et al., 2016) allow computing SO_2 plume height and thus correcting VCs. Here, to constrain plume height, we employed an alternative method called PlumeTraj which consists in a pixel-based trajectory analysis of an SO_2 cloud. Details of this approach can be found in Pardini et al. (2017, 2018) and in the Supplementary materials. Thus, only a brief summary is given here. A trajectory analysis is performed on the individual pixels composing the SO_2 cloud through the Hybrid Single-Particle Lagrangian Integrated Trajectory model, HYSPLIT (Stein et al., 2015). The outcomes of the trajectory computation are then used to compute the following parameters: the height (above sea level, asl) at which the SO_2 is located at satellite measurement time instant (hereafter plume height), the height at volcanic vent location at which the prevailing atmospheric current starts to disperse the gas into the atmosphere (hereafter injection height) and the time when the SO_2 reaches the injection height (hereafter injection time). All three quantities are 2D quantities and solved for the plume pixels only. The satellite data (containing an ensemble of images corresponding to VCs computed assuming a fixed number of SO_2 plume heights) is then corrected using the retrieved plume heights; i.e., the VCs are interpolated using the retrieved plume heights. From the three quantities and the corrected VCs for each plume pixel, the SO_2 load is computed. Since each pixel is associated with an injection time, a flux time-series can be derived by the algorithm. Furthermore, from the injection plume height time-series, PlumeTraj estimates the mass emission rate (*MER*) and the mass of solid erupted material (*M*)

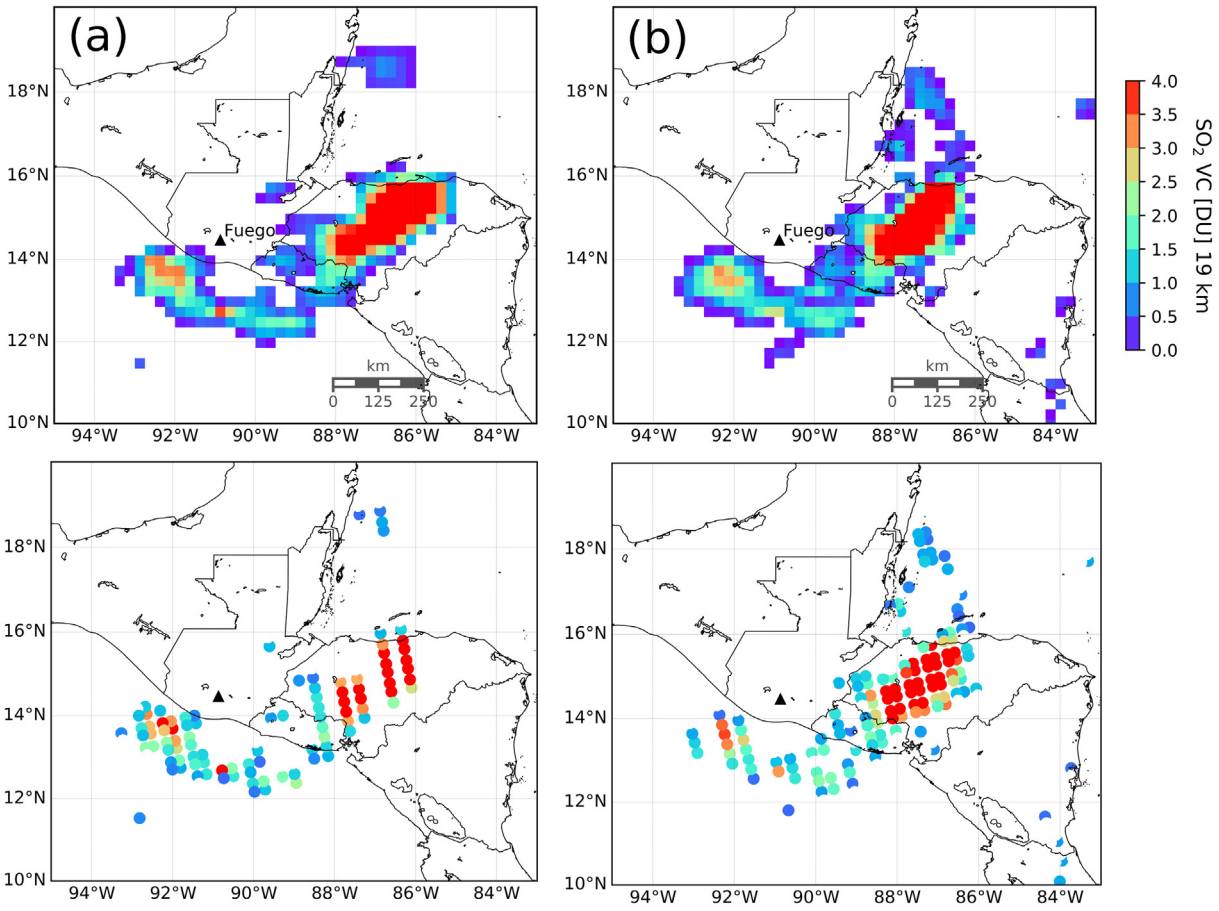

Fig. 2. SO_2 VCs from IASI assuming SO_2 located at 19 km asl, indicating a dispersing SO_2 plume drifting towards Southeast. (a) SO_2 as detected by IASI on board MetOp-A on 4 June 2018 at about 03:30 UTC. VCs are interpolated at 25 km grid used for PlumeTraj analysis. Corresponding VCs at IASI native spatial resolution are shown below. (b) Same as (a) but for IASI MetOp-B measurements, acquisition time 4 June 2018 at about 03:00 UTC. DU indicates Dobson units (1DU = 0.02848 g SO_2 m^{-2}).

by applying the well-known relationship between plume height and *MER* (Morton and Turner, 1956). To validate our numerically retrieved SO_2 plume height, we compared our results with those obtained by applying the plume height retrieval scheme based on infrared spectra presented in Clarisse et al. (2014).

For the present case study, meteorological data from the Global Forecast System (GFS) with quarter degree resolution (~25 km) was obtained from the website of the National Oceanic and Atmospheric Administration (https://www.ready.noaa.gov/archives.php). Following the resolution of the meteorological data, all satellite data are interpolated onto a 0.25° grid (about 25 km, Fig. 2).

Before running the trajectory analysis we used HYSPLIT in dispersion mode to allow for a better constraint on plume height (see Supplementary material, Text S2). Only then the actual back-trajectory analysis was performed using these constraints on plume height; that is, the backward trajectories were initialized from 7000 to 20,000 m only (see Supplementary material, Text S3). Finally, to test the consistency of our results, a further dispersal simulation was done using the numerically retrieved injection heights and SO_2 flux time-series as input values (Supplementary materials, Text S4).

Although widely used and a good approximation, the analytical relationship of Morton and Turner (1956) may provide quite inaccurate *MER* for real world plumes (Mastin et al., 2009). For an independent constraint on the *MER*, which helps to verify the trajectory model results, the integral column model PLUME-MoM was used (de' Michieli Vitturi et al., 2015). An inversion procedure was applied to PLUME-MoM to compute the best-fit *MER* starting from the plume height at the vent as retrieved by PlumeTraj. An uncertainty quantification technique has been implemented in the inversion procedure to assess the influence that input uncertainties (i.e., plume height to invert, gas content of the eruptive mixture, etc.) have on final *MER* (Supplementary materials, Text S5).

3. Results

Using PlumeTraj with pre-constrained initialization heights, as described above, allowed a more precise retrieval of the plume heights than an unconstrained initialization. Fig. 3 shows the retrieved plume heights, injection heights and injection times for the pixel of MetOp-B data (Fig. S6, Supplementary materials, for the corresponding results for MetOp-A). The injection heights (i.e., the initial plume bases) range between 13 and 20 km (Fig. 3b), and are associated with uncertainties around 1 km. Uncertainties (standard deviations, STD, Fig. 3d–f) were computed following the scheme detailed in Pardini et al. (2017) and are an estimate of how accurately the trajectories corresponding to a plume pixel originate from the vent. For comparison, plume heights retrieved with an independent algorithm (Clarisse et al., 2014) are shown in Fig. 3c (Fig. S6 for MetOp-A). Most heights agree with the plume heights from PlumeTraj within 1 STD, some (e.g., Northeastern part) within 2 STD. Fig. 4a and b show the SO_2 flux and injection height time-series for both MetOp-A and B data. Both MetOp-A and MetOp-B SO_2 flux time-series agree during the 2.5 h emission period with 13 ± 0.7 kt of SO_2 totally emitted. The symmetric shape of both time-series suggests a rapid increase in SO_2 flux peaking at 2400 kg s^{-1} at 18:30 UTC, after ~1 h of the short (~2.5 h) climactic paroxysmal phase of the eruption. While the eruption began at ~06:00 UTC, the initial activity was not detected by IASI for reasons detailed in the Discussion or because the SO_2 load emitted was below IASI's detection

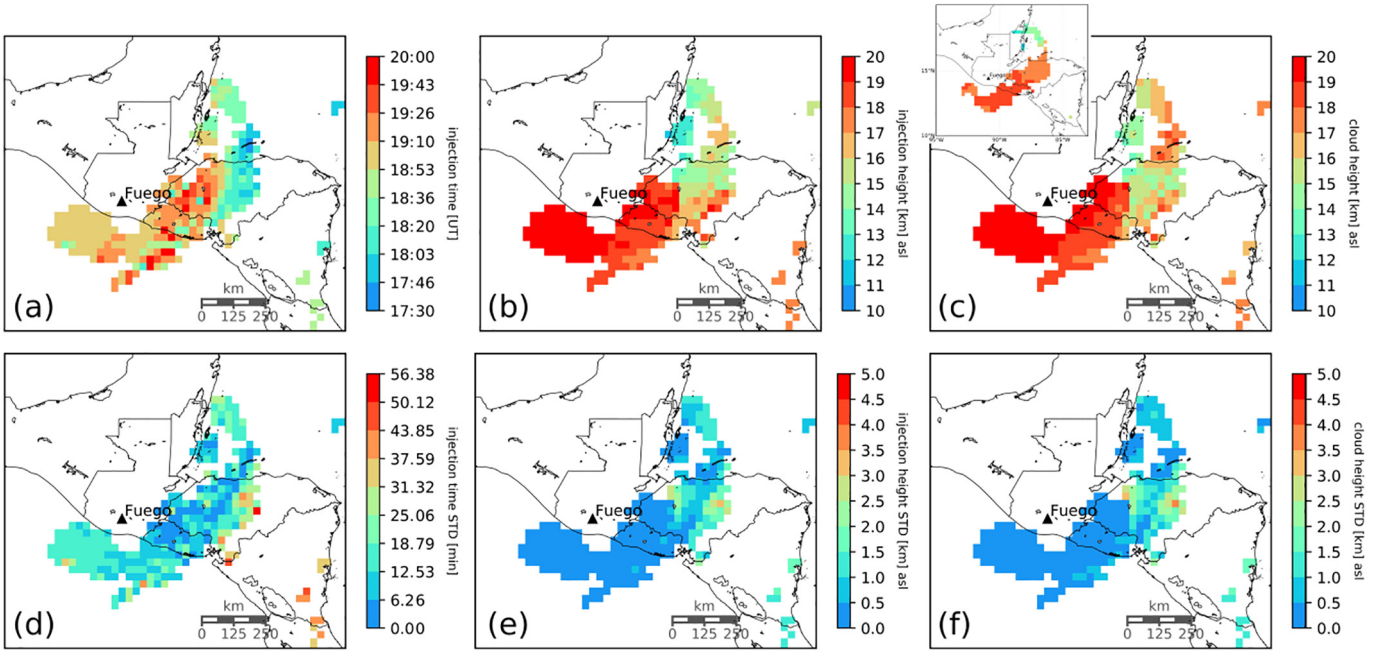

Fig. 3. Results for the IASI MetOp-B observations. (a) Injection times. (b) Injection heights. (c) Plume (cloud) heights. Inset: Plume heights from retrieval method by Clarisse et al. (2014). (d)–(f) show the respective standard deviations.

limit. The retrieval algorithm used for the IASI data is associated with an approximate SO_2 detection limit of 0.5 DU on a per pixel basis (Clarisse et al., 2012).

The mean injection height during the eruption (Fig. 4b) of around 17.5 km asl varies only moderately with time, indicating a direct injection of volcanic volatiles at the tropopause level. The retrieved *MER* of $1.17 \pm 0.14 \times 10^7$ kgs^{-1} was used to compute a dense rock equivalent (*DRE*) of 0.03 ± 0.004 km^3 (Table 1), assuming a magma density of 2830 kg m^{-3}, as determined for Fuego volcano (Whittington et al., 2013). The erupted solid mass of ~100 Mt and the total erupted SO_2 mass of 13 kt suggest an SO_2 content of ~0.013 wt%, equivalent to 65 ppm S (Table 1). Using the injection height time-series obtained from PlumeTraj, PLUME-MoM was used to invert for *MER* (Fig. 4c). The mean over all *MER* gives $1.39 \pm 0.33 \times 10^7$ kg s^{-1}, in reasonable agreement with the *MER* previously computed by PlumeTraj (Table 1). *DRE* and SO_2 content inferred from PLUME-MoM inversion are 0.04 ± 0.01 km^3 and 0.01 ± 0.002 wt% respectively. The latter is equivalent to 50 ppm of magmatic S.

While care has been taken to obtain an accurate estimate of *MER* it should be noted that for tropical eruptions, such as the present event, atmospheric instability, high moisture content and convection can generate significant plume altitudes from relatively low *MER*s. The paroxysmal phase of the June 2018 Fuego eruption occurred around noon in the tropics, so it is likely that atmospheric instability (latent heat, etc.) influenced the plume altitude. This is not accounted for by PLUME-MoM. Hence, *MER* and *DRE* in Table 1 likely represent an upper limit and the S content a lower limit. This is detailed in the Discussion section below.

4. Discussion

To increase accuracy of the retrieved SO_2 burden and *MER*, a strategy could be to use all available passages of all satellites and to reconstruct a time-lapse evolution of SO_2 flux near the source, which could enable detecting major atmospheric sinks such as scavenging. Indeed, a number of UV and IR sensors onboard satellite platforms are currently employed for the daily detection of volcanic SO_2 (McCormick et al., 2013) and they can provide multiple SO_2 acquisitions per day. However, depending on the atmospheric conditions at a given pixel location and the instrument type (e.g., spectral region), the precision and accuracy of these estimates will to some extent still suffer from atmospheric effects, e.g., cloud cover or light dilution by volcanic ash. The eruption of Fuego, a volcano in a moist and instable tropical atmosphere, poses a challenge for optical satellite remote sensors, such as due to interference from clouds. Indeed, our estimates of S content of 50 to 65 ppm (Table 1) appear very low for a basaltic arc volcano (Wallace, 2001) and much lower than those reported by authors studying the 1974 eruption. Lloyd et al. (2013, 2014) report melt inclusion data with peak S content of ~2500 ppm for the most intense 17 October 1974 eruption, whose plume reached a similar height to the June 2018 event. Ash composition (Rose et al., 1978), crystal size distribution (Roggensack, 2001) and volatile contents varied between individual events of the 1974 eruption sequence, suggesting magma heterogeneity, but the 17 October 1974 event appeared to have been driven by a simple influx of fresh basaltic melt (Lloyd et al., 2013, 2014) with a S content up to 2500 ppm.

As will be examined in the following, atmospheric optical effects and physiochemical removal of atmospheric SO_2 can lead to significant underestimations of SO_2 amount retrieved from space. Firstly, satellite detection of volcanic SO_2 suffers from meteorological clouds and ash cover. Ash and cloud layers can alter the spectral signal measured by the sensor. The SO_2 load retrieved from IASI measurements can be severely underestimated if the SO_2 cloud is located within a meteorological cloud layer (Carboni et al., 2012). Figs. 1b and S4 indicate dense cloud cover near the vent. Fig. S9 indicates ice formation. Downwind from the vent, cloud fractions of 1 for most of the pixels collocated with the plume dominated, with cloud top heights between 9 and over 12 km, retrieved from MODIS Aqua and Terra (Platnick et al., 2015). Given the retrieved plume height, this indicates that parts of the SO_2 plume were within the meteorological cloud layer. Sensitivity tests with synthetic IASI spectra (Carboni et al., 2012), assuming a 20 μm effective droplet radius, have shown that for optical depths (OD) of 1.0 (at 550 nm) SO_2 columns are underestimated by a factor of ~2, while for OD of 5 (at 550 nm) SO_2 columns would be underestimated by a factor of ~5. Optical densities retrieved from MODIS Aqua instrument indicate a minimum OD of 5 and localized maxima of 40 (Platnick et al., 2015), which would make SO_2 undetectable for IASI. The MODIS OD have been retrieved for a wavelength of 1.6 μm (band 6). Mie backscattering calculations, assuming spherical droplets in air with an effective 20 μm radius, result in a decrease in extinction

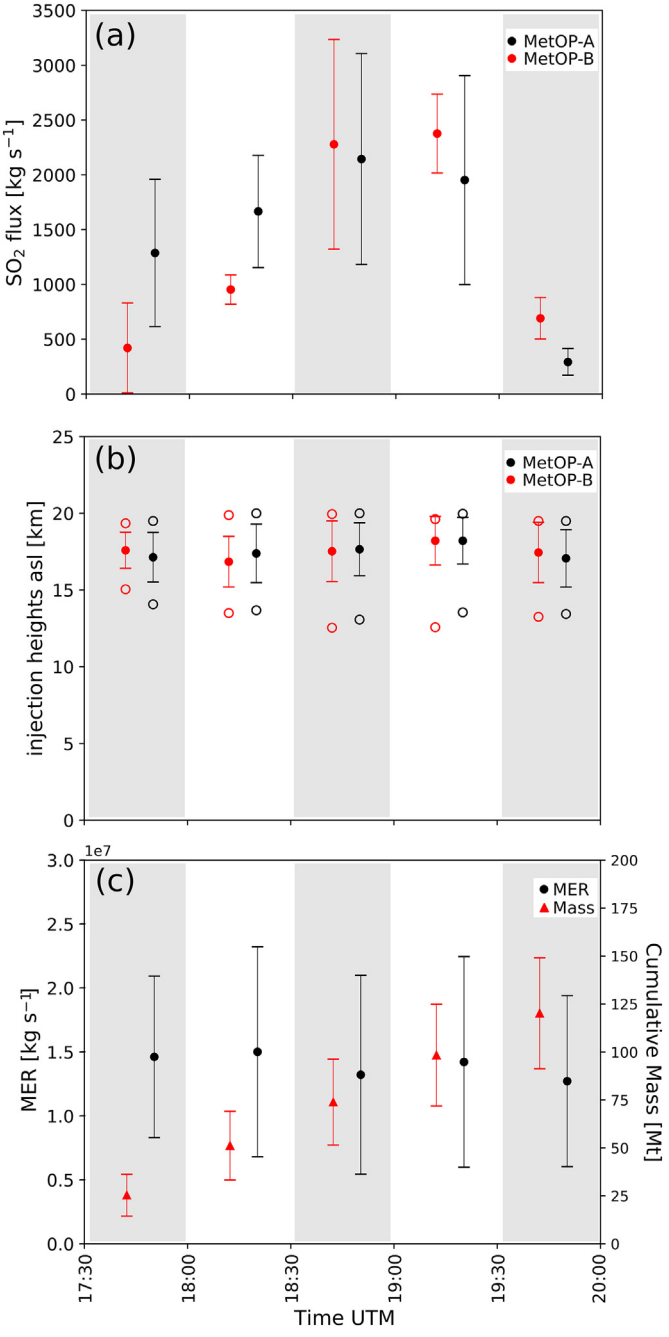

Fig. 4. Time-series derived from the results displayed in Fig. 3 for MetOp-B and in Fig. S6 (Supplementary material) for MetOp-A. Each grey bar indicates a 30 min time window. (a) SO_2 flux time-series from both the MetOp-A and MetOp-B results. A good match between the two time-series can be observed with fluxes peaking at ~2400 kg s^{-1} 1 h after the beginning of the climactic phase. Differences between the two time-series, especially during the first hour, reflect the differences in the satellite datasets used to compute the fluxes. Indeed, differences between the SO_2 cloud as seen by MetOp-A and -B can be observed in Fig. 2. (b) Mean injection height time-series. The hollow circles mark minimum and maximum. The error bars are computed using the standard deviations shown in Fig. 3. Values for MetOp-B have the same time instant as those for MetOp-A but are plotted staggered for better display. (c) Mass emission rate time-series obtained from PLUME-MoM (see Table S4 for values used). Shown is the *MER* with standard deviations and the cumulative solid mass erupted (triangles).

coefficient by only 19% when moving to 550 nm. Therefore, a minimum underestimation of SO_2 load by a factor of 5 for all plume pixels is adopted here (Table 2). Ash also yields underestimated SO_2 columns. For ash optical densities above 2.0 (for 550 nm wavelength and for 2 μm effective radius, which is within range of ash particle sizes of the Fuego 1974 eruption (Rose et al., 2008)), the SO_2 load is underestimated by 50% and for optical depths >5 it is masked completely. Optical densities from MODIS Terra for the plume location are ~0.3 (at 550 nm, Levy et al., 2015), which suggests that light attenuation by ash has had an insignificant effect on SO_2 retrieval (Carboni et al., 2012).

Secondly, atmospheric removal processes, such as SO_2 conversion into sulfate aerosol and scavenging mechanisms, can deplete part of the SO_2 originally emitted. Indeed, for the Fuego eruption, conversion of SO_2 into sulfate aerosol, H_2SO_4, and subsequent absorption of H_2SO_4 into ash particles may have efficiently removed SO_2 from the plume, especially for older parts of the plume (Crafford, 1975; Rose, 1977; Oppenheimer et al., 1998; McGonigle et al., 2004). Over 33% of S emitted during one of the pulses of the 1974 Fuego eruptive sequence was possibly removed in this way (Rose, 1977). Since the 3 June 2018 eruption was ash rich the same order of magnitude of S could likely have been removed (Table 2).

The 1974 eruption occurred towards the end of the wet season (October), while the 2018 eruption occurred during the wet season; therefore, the atmosphere had a high moisture content. The GOES images (Fig. S4 in Supplementary materials) indicate water- or ice-rich clouds. The dew point of −9 °C during the 1974 eruption versus −4 °C during the 2018 eruption (http://www.ncdc.noaa.gov) suggests even higher moisture content during the 2018 eruption and liquid water within the plume. Sulfur species are only slightly soluble in liquid water, but may efficiently be incorporated into ice particles (Textor et al., 2003). Entrainment of ambient water vapour is a crucial part of the development of an eruption plume. The high atmospheric moisture along with ash particles content therefore favoured creation of ice particles within the colder parts of the eruption column. Solid clusters of ash and hydrometeors may fall out and remove SO_2 from the plume (Herzog et al., 1998). Numerical modeling of a volcanic eruption with similar volcanic parameters under tropical conditions yielded substantial ice formation from condensed cloud water droplets half an hour after eruption onset, between heights of 8 and 16 km (at SO_2 plume level), 2 km away from the eruption column, with the ice phase dominating over liquid cloud water (Herzog et al., 1998). This scavenging by ice particles was likely another key S removal mechanism. Numerical modeling for an ideal Plinian eruption in a subtropical atmosphere yielded a 20% removal of S-species (Textor et al., 2003), which yields a lower limit underestimation factor of SO_2 (Table 2).

Overall, we quantified ash and cloud cover together with scavenging mechanisms to give rise to an underestimation of SO_2 atmospheric yield by an order of magnitude (Table 2) with respect to the value of 13 kt originally measured by IASI; hence the total SO_2 load emitted was likely at least ~130 kt. The change in atmospheric SO_2 loading from 13 to 130 kt does not alter the value of *MER* computed by PLUME-MoM (*MER* depends on column height only), while it influences the estimate of magmatic S content and, potentially, *DRE*.

Considering 130 kt of SO_2 and 1.39 ± 0.33 kg s^{-1} of material erupted during the 2.5 h climactic phase, the magmatic S content was likely at least 500 ppm, while *DRE* remains equal to 0.04 km^3 (the total amount of S is still too low to have significant impact on DRE).

Modeling results suggest the release of latent heat due to condensation of entrained water vapour to provide additional plume uplift (Herzog et al., 1998). For large Plinian eruptions ($MER > 10^7$ kg s^{-1}), however, latent heat was found to be small compared to thermal energy of the plume (Woods, 1993). Even though it may be relatively small, both models agree on the fact that additional plume uplift due to latent heat would take place. For a Plinian eruption in a tropical atmosphere an additional uplift of 1500 m is possible (Herzog et al., 1998), which, using the empirical relationship between *MER* and plume height (Morton and Turner, 1956) would entail an *MER* overestimated and a S content underestimated by a factor of 1.6.

Thus, rather than 50 ppm (Table 1), the S content of the 2018 Fuego eruption was likely between 500 and 800 ppm, possibly higher. This figure is in line with the lower limit of S concentrations found for the 1974 eruption (600–2500 ppm, Lloyd et al., 2013, 2014). From this

Table 1
Main parameters obtained from PlumeTraj and PLUME-MoM where applicable. *M* and *DRE* indicate the mass of solid material erupted and the Dense Rock Equivalent assuming a water vapour content in the range 2–6 wt% and an eruption duration of 2.5 h (most intense phase). The SO_2 mass loading represents the mean from the results for MetOp-A and MetOp-B. Implied elemental S contents are therefore 65 ppm for PlumeTraj and 50 ppm for PLUME-MoM (see Discussion for final values).

	Mean plume height (km)	*MER* ($\times 10^7$ kg s^{-1})	*M* (Mt)	*DRE* (km^3)	Min./Max. SO_2 flux (kg s^{-1})	SO_2 mass loading (kt)	SO_2 content (wt%)
PlumeTraj	17.5 ± 2.4	1.17 ± 0.14	100 ± 12	0.03 ± 0.004	293 ± 121/2376 ± 359	13 ± 0.7	0.013 ± 0.006
PLUME-MoM	NA	1.39 ± 0.33	120 ± 29	0.04 ± 0.01	NA	NA	0.01 ± 0.002

consideration we cannot exclude that the 2018 eruption may have been triggered by the influx of fresh basaltic magma similar to the 1974 eruption. However, in the light of Fuego's past eruptive behavior, below we propose an alternative triggering mechanism for the 3 June 2018 eruption coherent with a relatively low S content retrieved by our numerical/satellite analysis.

The eruptive history of Fuego is characterized by occasional, large-magnitude (VEI 4) eruptions occurring every 40 to 70 years, e.g., in 1880, 1932, 1971, and 1974 (Deger, 1932; Rose et al., 1978; Lyons et al., 2010). These large-magnitude eruptions occur against a quasi-permanent background of persistent Strombolian activity and ash-rich explosive eruptions (Lyons et al., 2010; Nadeau et al., 2011). The most recent eruptive regime of Fuego began with a VEI 2 eruption on 21 May 1999 (Lyons et al., 2010; Waite et al., 2013), and activity between that date and the present day has been dominated by persistent Strombolian activity and open-vent conditions. This activity is interspersed with frequent paroxysmal eruptions, producing ash-rich explosions and lava flows, with occasional pyroclastic flows (e.g., the paroxysmal eruption of 5 May 2017). Latest findings evidence a new phase of increased frequency in paroxysmal activity at Fuego since 2015 (Naismith et al., 2019). The 3 June 2018 eruption was, both by *DRE* erupted volume and impact on surrounding populations, the largest paroxysmal eruption of the current eruptive regime. In *DRE* volume it is analogous to an individual event within the October 1974 eruptive cluster. Indeed, our estimate of 0.04 ± 0.01 km^3 *DRE* is in line with the ~0.02 km^3 *DRE* estimated by Rose et al. (2008) for the first pulse of the 1974 eruptive cycle. Thus, the 3 June 2018 eruption is comparable with the largest-magnitude eruptions that characterize Fuego's longer eruptive history. The events of 1974 have shown that Fuego is capable of producing a series of large-magnitude eruptions in a short time. However, although the 3 June 2018 eruption was dissimilar to previous paroxysms in the current eruptive regime in that it did not produce lava flows, this does not necessarily mean that this represents a change in the eruptive regime going forward. The large populations that live on Fuego's flanks are still vulnerable to future large-magnitude eruptions; continued monitoring of the volcano's activity, whether it continues in the same eruptive regime or not, is essential.

The 3 June 2018 eruption began as a typical paroxysm at 12:00 UTC but then rapidly accelerated towards a ~2.5 hour period climactic paroxysmal episode between 17:30 and 20:00 UTC, with a maximum SO_2 flux at least three orders of magnitude above quiescent levels (Fig. 2, Rodríguez et al., 2004). The estimated total *DRE* volume of around 0.04 km^3 (Table 1) compares well to the *DRE* of 0.02 km^3 that was estimated from one of the four events produced in the 1974 eruption sequence, which overall produced ~0.1 km^3 of tephra and pyroclastic flow material (Riley et al., 2003; Rose et al., 2008). The height of the eruptive column on 3 June was between 13 and 20 km (~17.5 km on average, Table 1). VAAC reported a plume height of ~15 km in agreement of the present finding (VAAC, 2018). Lidar backscattering from CALIPSO acquired at 07:50 UTC (~5 h after IASI overpass) suggests a cloud between 16 and 18 km altitude (Fig. S9, Supplementary materials). This height is comparable to the 13 to 17 km reported for the largest of the 1974 eruptions (Rose et al., 2008). As in 1974, no extensive lava flow was produced, but large pyroclastic flows (Davies et al., 1978; Global Volcanism Program, 2018a, b) were generated. The proportion of the total *DRE* volume erupted as pyroclastic flows in the 3 June eruption is uncertain, but in volume is likely to be intermediate between the flows produced in the October 1974 eruptive cluster (e.g., 0.0039 km^3 on 14th October (Rose et al., 2008)) and those produced in the September 1971 eruption (>0.06 km^3 (Rose et al., 1978)) – noting in the case of the October 1974 cluster that the vast majority of erupted volume was as tephra (Davies et al., 1978). The high rising eruptive column and the fairly constant mean injection height (Fig. 4b) indicate a sustained steady eruption during the ~2.5 h climactic paroxysmal phase. While a mild bell shape can be seen in the SO_2 flux (Fig. 4a), this is also relatively constant during the paroxysmal phase.

The development of the 3 June eruption is highly unusual for Fuego and requires some consideration. The eruption began with explosive activity, similar to that observed in Fuego's recent history, at 06:00 local time (12:00 UTC), producing an incandescent fountain and pyroclastic flows that descended the W flanks of Fuego. Unusually for recent fountains, the event did not appear to be preceded by lava flow effusion, although extremely poor visibility due to cloud could have obscured short lava flows on the upper flanks. What was particularly different about this eruption was its sudden acceleration, starting after 11:30 local time (17:30 UTC), producing a tall eruption column and a rapid series of pyroclastic flows directed towards the E flanks (Global Volcanism Program, 2018a, b).

Significant variability in S content has been observed in previous eruptions, such as 1932 versus 1974 (Berlo et al., 2012), and this may be interpreted as different degrees of shallow storage prior to eruption. If the 3 June eruption has not been triggered by influx of fresh basaltic magma, then alternatively, and in line with our relatively low bulk S content and steady eruption style, the June 3 paroxysm could have been powered by shallow magma which had lost much of its S, and whose powering volatile composition was probably rich in H_2O (supported by a plume appearing water rich in Fig. S4) and potentially CO_2 fluxing from deeper in the plumbing system. We highlight the possibility that accumulated excess volatiles other than SO_2 could have triggered the eruption and a clearing of the volcanic throat (Allard et al., 2005). Although this could be a viable mechanism, it remains a speculation. Petrological analysis of the deposits is required to independently constrain the original S content for magmas driving the June 2018 eruption (e.g., Wallace, 2001; Sigmarsson et al., 2013), as well as the abundance of other major magmatic gases such as water vapour and CO_2.

The cyclic activity pattern observed in Fuego involves the convolution of several processes associated with a continuous transition from opened to closed degassing evidenced by modulations on the flux of volatiles such as SO_2 (Rodríguez et al., 2004) and a pulsatory activity (Martin and Rose, 1981). As water vapour exsolves from the rising, mainly basaltic magma, the crystal content increases and so does the viscosity of the magma (Caricchi et al., 2007), which is further boosted

Table 2
SO_2 removal effects during the Fuego eruption and lower limit of contribution to underestimated SO_2 flux. The total underestimation factor is the product of all three factors.

Removal mechanism	Underestimation factor
Meteorological clouds	5.00
Scavening by ash	1.50
Scavenging by ice	1.25
Total	9.5

by strong magma cooling due to gas expansion (La Spina et al., 2015). Based on a water content of 5 wt% at depth, Lyons and Waite (2011) estimated an undercooling of 80 K near the surface, implying high crystal growth rates, which may be consistent with production of crystal-rich products observed from previous eruptions (Berlo et al., 2012). However, a fast ascent rate such as that calculated for the 1974 eruption (Lloyd et al., 2014) may also inhibit crystallization as there may be insufficient time to crystallize (La Spina et al., 2015). Detailed examination of the eruption products will help to elucidate the eruption process. A key question is what drives the transition to a paroxysmal phase from the relatively benign explosive activity that typifies Fuego. Perhaps a relatively small acceleration in eruption rate can reduce the time allowed for crystal growth to occur, entering into a positive feedback process where faster ascent produces fewer crystals, which leads to lower viscosity and still faster ascent. This could therefore trigger the paroxysmal phase, which then ends when the magma chamber is sufficiently emptied such that the pressure is reduced. Alternatively, a brittle seal in the upper part of the magma column could lead to a large pressure build-up followed by a rapid depressurization upon brittle failure of the sealing plug. A qualitatively similar cycling mechanism seems to occur at timescales of days (leading to small-scale explosive activity (Nadeau et al., 2011)) up to at least years (Lyons and Waite, 2011).

5. Conclusions and perspectives

Analysis of IASI satellite data provided essential eruption parameters, such as plume height, SO_2 flux time-series and magma sulfur content. These allowed initial insights into source mechanisms driving the eruption of Fuego from 3 June 2018 to be part of a ~45-year cycle of high-energy eruptions that exhibit high erupted volumes, high rising eruptive columns and long reaching pyroclastic flows. The extraordinary eruption intensity of the 2018 eruption, appears to have been driven by magma with a minimum sulfur content of 500 ppm. This suggests a triggering mechanism similar to the 1974 eruption (influx of fresh magma). Challenging atmospheric conditions for satellite remote sensing meant that most of the SO_2 emitted was undetectable by IASI and only a lower limit S content could be determined. The lack of an upper limit on S content allows for the possibility of an eruption to be driven by shallow magma which had lost much of its S, and whose powering volatile composition could have been rich in H_2O (supported by a plume appearing water rich) and potentially CO_2 fluxing from deeper in the plumbing system. Detailed petrological analysis of eruption products is needed to further elucidate the source mechanisms of the 3 June 2018 eruption of Fuego volcano.

With the onset of new, more powerful satellite remote sensing platforms in coming months and years to detect SO_2 (Theys et al., 2017) and potentially CO_2, a relatively effortless detailed time-series of gas flux can be acquired using techniques such as PlumeTraj and HYSPLIT trajectory modeling, which allow timely interpretations of eruptive styles following explosive eruptions.

Acknowledgments, samples, and data

We thank two anonymous reviewers for their substantial and productive critics. The research leading to these results has received funding from the European Research Council Proof-of-Concept Grant CarbSens (ERC-2016-PoC agreement no. 727626). We gratefully acknowledge funding support from the European Research Council under the European Union Seventh Framework Programme (FP/2007–2013)/ERC Grant Agreement no. 279802 and from RCUK NERC DisEqm project (NE/N018575/1). L.C. is a research associate supported by the Belgian Fonds de la Recherche Scientifique (F.R.S.-FNRS). We thank Fabio Arzilli for very helpful discussions and input. The data acquired is stored in the University of Manchester's research data repository and may be requested by contacting mike.burton@manchester.ac.uk. The authors declare no conflict of interest.

Appendix A. Supplementary data

Supplementary data to this article can be found online at https://doi.org/10.1016/j.jvolgeores.2019.03.014.

References

Allard, P., Burton, M., Muré, F., 2005. Spectroscopic evidence for a lava fountain driven by previously accumulated magmatic gas. Nature 433, 407–410. https://doi.org/10.1038/nature03246.

Berlo, K., Stix, J., Roggensack, K., Ghaleb, B., 2012. A tale of two magmas, Fuego, Guatemala. Bull. Volcanol. 74, 377–390. https://doi.org/10.1007/s00445-011-0530-8.

Carboni, E., Grainger, R., Walker, J., Dudhia, A., Siddans, R., 2012. A new scheme for sulphur dioxide retrieval from IASI measurements: application to the Eyjafjallajökull eruption of April and May 2010. Atmos. Chem. Phys. 12 (23), 11417–11434.

Carboni, E., Grainger, R., Mather, T.A., Pyle, D.M., Dudhia, A., Thomas, G., Siddans, R., Smith, A., Koukouli, M., Balis, D., 2016. The vertical distribution of volcanic SO_2 plumes measured by IASI. Atmos. Chem. Phys. 16, 4343–4367.

Caricchi, L., Burlini, L., Ulmer, P., Gerya, T., Vassalli, M., Papale, P., 2007. Non-Newtonian rheology of crystal-bearing magmas and implications for magma ascent dynamics. Earth Planet. Sci. Lett. 264 (3), 402–419.

Carn, S.A., Clarisse, L., Prata, A.J., 2016. Multi-decadal satellite measurements of global volcanic degassing. J. Volcanol. Geotherm. Res. 311, 99–134.

Chesner, C.A., Rose, W.I., 1984. Geochemistry and evolution of the Fuego volcanic complex, Guatemala. J. Volcanol. Geotherm. Res. 21, 25–44.

Clarisse, L., Hurtmans, D., Clerbaux, C., Hadji-Lazaro, J., Ngadi, Y., Coheur, P.F., 2012. Retrieval of sulphur dioxide from the infrared atmospheric sounding interferometer (IASI). Atmos. Meas. Tech. 5 (3), 581–594.

Clarisse, L., Coheur, P.F., Theys, N., Hurtmans, D., Clerbaux, C., 2014. The 2011 Nabro eruption, a SO_2 plume height analysis using IASI measurements. Atmos. Chem. Phys. 14 (6), 3095–3111.

CONRED, 2018. FLUJOS PIROCLÁSTICOS EN BARRANCA LAS LAJAS: De acuerdo al boletín especial número 38-2018 emitido por el INSIVUMEH, hace unos momentos en el volcán de Fuego se iniciaron a generar flujos piroclásticos en dirección a la Barranca Las Lajas. Es importante guardar la calma, 5 June 2018 Tweet. https://twitter.com/conredguatemala/status/1004197725137788928?lang=en, Accessed date: 21 August 2018.

Crafford, T.C., 1975. SO_2 emission of the 1974 eruption of Volcan Fuego, Guatemala. Bull. Volcanol. 39, 536. https://doi.org/10.1007/BF02596975.

Davies, D.K., Quearry, M.W., Bonis, S.B., 1978. Glowing avalanches from the 1974 eruption of the volcano Fuego, Guatemala. Geol. Soc. Am. Bull. 89, 369–384.

de' Michieli Vitturi, M., Neri, A., Barsotti, S., 2015. PLUME-MoM 1.0: a new integral model of volcanic plumes based on the method of moments. Geosci. Model Dev. 8, 2447–2463. https://doi.org/10.5194/gmd-8-2447-2015.

Deger, E., 1932. Der Ausbruch des Vulkans Fuego in Guatemala am 21 Januar 1932 und die chemische Zusammensetzung seiner Auswurfsmaterialien. Chem. Erde 7 (2), 291–297.

Efremenko, D.S., Loyola, R.D.G., Hedelt, P., Spurr, R.J., 2017. Volcanic SO_2 plume height retrieval from UV sensors using a full-physics inverse learning machine algorithm. Int. J. Remote Sens. 38 (Suppl. 1), 1–27.

Flemming, J., Inness, A., 2013. Volcanic sulfur dioxide plume forecasts based on UV satellite retrievals for the 2011 Grímsvötn and the 2010 Eyjafjallajökull eruption. J. Geophys. Res. Atmos. 118, 10172–10189. https://doi.org/10.1002/jgrd.50753.

Global Volcanism Program, 2018a. Report on Fuego (Guatemala). In: Sennert, S.K. (Ed.), Weekly Volcanic Activity Report, 30 May–5 June 2018. Smithsonian Institution and US Geological Survey.

Global Volcanism Program, 2018b. Report on Fuego (Guatemala). In: Sennert, S.K. (Ed.), Weekly Volcanic Activity Report, 6 June–12 June 2018. Smithsonian Institution and US Geological Survey.

Heard, I.P.C., Manning, A.J., Haywood, J.M., Witham, C., Redington, A., Jones, A., Clarisse, L., Bourassa, A., 2012. A comparison of atmospheric dispersion model predictions with observations of SO_2 and sulphate aerosol from volcanic eruptions. J. Geophys. Res. Atmos. 117, D00U22. https://doi.org/10.1029/2011JD016791.

Heng, Y., Hoffmann, L., Griessbach, S., Rößler, T., Stein, O., 2016. Inverse transport modeling of volcanic sulfur dioxide emissions using large-scale simulations. Geosci. Model Dev. 9 (4).

Herzog, M., Graf, H.F., Textor, C., Oberhuber, J.M., 1998. The effect of phase changes of water on the development of volcanic plumes. J. Volcanol. Geotherm. Res. 87 (1–4), 55–74.

Hughes, E.J., Sparling, L.C., Carn, S.A., Krueger, A.J., 2012. Using horizontal transport characteristics to infer an emission height time series of volcanic SO_2. J. Geophys. Res. Atmos. 117 (D18).

La Spina, G., Burton, M., de' Michieli Vitturi, M., 2015. Temperature evolution during magma ascent in basaltic effusive eruptions: a numerical application to Stromboli volcano. Earth Planet. Sci. Lett. 426, 89–100. https://doi.org/10.1016/j.epsl.2015.06.015.

Levy, R.C., Munchak, L.A., Mattoo, S., Patadia, F., Remer, L.A., Holz, R.E., 2015. Towards a long-term global aerosol optical depth record: applying a consistent aerosol retrieval algorithm to MODIS and VIIRS-observed reflectance. Atmos. Meas. Tech. 8 (10), 4083–4110.

Lloyd, A.S., Plank, T., Ruprecht, P., Hauri, E.H., Rose, W., 2013. Volatile loss from melt inclusions in pyroclasts of differing sizes. Contrib. Mineral. Petrol. 165 (1), 129–153.

Lloyd, A.S., Ruprecht, P., Hauri, E.H., Rose, W., Gonnermann, H.M., Plank, T., 2014. NanoSIMS results from olivine-hosted melt embayments: magma ascent rate during explosive basaltic eruptions. J. Volcanol. Geotherm. Res. 283, 1–18.

Lyons, J.J., Waite, G.P., 2011. Dynamics of explosive volcanism at Fuego volcano imaged with very long period seismicity. J. Geophys. Res. Solid Earth 116, B09303. https://doi.org/10.1029/2011JB008521.

Lyons, J.J., Waite, G.P., Rose, W.I., Chigna, G., 2010. Patterns in open vent, strombolian behavior at Fuego volcano, Guatemala, 2005–2007. Bull. Volcanol. 72 (1), 1.

Martin, D.P., Rose, W.I., 1981. Behavioral patterns of Fuego volcano, Guatemala. J. Volcanol. Geotherm. Res. 10 (1–3), 67–81. https://doi.org/10.1016/0377-0273(81)90055-X.

Mastin, L.G., Guffanti, M., Servranckx, R., Webley, P., Barsotti, S., Dean, K., Durant, A., Ewert, J.W., Neri, A., Rose, W.I., Schneider, D., Siebert, L., Stunder, L., Swanson, G., Tupper, A., Volentik, A., Waythomas, C.F., 2009. A multidisciplinary effort to assign realistic source parameters to models of volcanic ash-cloud transport and dispersion during eruptions. J. Volcanol. Geotherm. Res. 186, 10–21.

McCormick, B., Edmonds, M., Mather, T.A., Campion, R., Hayer, C.S.L., Thomas, H.E., Carn, S.A., 2013. Volcano monitoring applications of the Ozone Monitoring Instrument. Geol. Soc. Lond., Spec. Publ. 380, SP380–11. https://doi.org/10.1144/SP380.11.

McGonigle, A.J.S., Delmelle, P., Oppenheimer, C., Tsanev, V.I., Delfosse, T., Williams-Jones, G., Horton, K., Mather, T.A., 2004. SO_2 depletion in tropospheric volcanic plumes. Geophys. Res. Lett. 31 (13).

Morton, B.R., Turner, J.S., 1956. Turbulent gravitational convection from maintained and instantaneous sources. Proc. R. Soc. Lond. A 234 (1196) (The Royal Society).

Nadeau, P.A., Palma, J.L., Waite, G.P., 2011. Linking volcanic tremor, degassing, and eruption dynamics via SO_2 imaging. Geophys. Res. Lett. 38 (1), L01304. https://doi.org/10.1029/2010GL045820.

Naismith, A.K., Watson, I.M., Escobar-Wolf, R., Chigna, G., Thomas, H., Coppola, D., Chun, C., 2019. Eruption frequency patterns through time for the current (1999–2018) activity cycle at Volcán de Fuego derived from remote sensing data: evidence for an accelerating cycle of explosive paroxysms and potential implications of eruptive activity. J. Volcanol. Geotherm. Res. 371, 206–219. https://doi.org/10.1016/j.jvolgeores.2019.01.001.

Oppenheimer, C., Francis, P., Stix, J., 1998. Depletion rates of sulfur dioxide in tropospheric volcanic plumes. Geophys. Res. Lett. 25 (14), 2671–2674.

Pardini, F., Burton, M., Vitturi, M.D.M., Corradini, S., Salerno, G., Merucci, L., Di Grazia, G., 2017. Retrieval and intercomparison of volcanic SO_2 injection height and eruption time from satellite maps and ground-based observations. J. Volcanol. Geotherm. Res. 331, 79–91. https://doi.org/10.1016/j.jvolgeores.2016.12.008.

Pardini, F., Burton, M., Arzilli, F., La Spina, G., Polacci, M., 2018. SO_2 emissions, plume heights and magmatic processes inferred from satellite data: the 2015 Calbuco eruptions. J. Volcanol. Geotherm. Res. 361, 12–24.

Platnick, S., Ackerman, S., King, M., Meyer, K., Menzel, W.P., Holz, R.E., Baum, B.A., Yang, P., 2015. MODIS Atmosphere L2 Cloud Product (06_L2). NASA MODIS Adaptive Processing System. Goddard Space Flight Center, USA https://doi.org/10.5067/MODIS/MOD06_L2.006.

Riley, C.M., Rose, W.I., Bluth, G.J.S., 2003. Quantitative shape measurements of distal volcanic ash. J. Geophys. Res. Solid Earth 108 (B10), 2504. https://doi.org/10.1029/2001JB000818.

Rix, M., Valks, P., Hao, N., Loyola, D., Schlager, H., Huntrieser, H., Flemming, J., Koehler, U., Schumann, U., Inness, A., 2012. Volcanic SO_2, BrO and plume height estimations using GOME-2 satellite measurements during the eruption of Eyjafjallajökull in May 2010. J. Geophys. Res. Atmos. 117 (D20).

Rodríguez, L.A., Watson, M., Rose, W.I., Branan, Y.K., Bluth, G.J.S., Chigna, G., Matias, O., Escobar, D., Carn, S., Fischer, T.P., 2004. SO_2 emissions to the atmosphere from active volcanoes in Guatemala and El Salvador, 1999–2002. J. Volcanol. Geotherm. Res. 138 (3), 325–344. https://doi.org/10.1016/j.jvolgeores.2004.07.008.

Roggensack, K., 2001. Unraveling the 1974 eruption of Fuego volcano (Guatemala) with small crystals and their young melt inclusions. Geology 29 (10), 911–914. https://doi.org/10.1130/0091-7613(2001)029<0911:UTEOFV>2.0.CO;2.

Rose, W.I., 1977. Scavenging of volcanic aerosol by ash: atmospheric and volcanologic implications. Geology 5, 621. https://doi.org/10.1130/0091-7613(1977)5<621:SOVABA>2.0.CO;2.

Rose, W.I., Anderson, A.T., Woodruff, L.G., Bonis, S.B., 1978. The October 1974 basaltic tephra from Fuego volcano: description and history of the magma body. J. Volcanol. Geotherm. Res. 4 (1–2), 3–53. https://doi.org/10.1016/0377-0273(78)90027-6.

Rose, W.I., Self, S., Murrow, P.J., Bonadonna, C., Durant, A.J., Ernst, G.G.J., 2008. Nature and significance of small volume fall deposit at composite volcanoes: insights from the October 14, 1974 Fuego eruption, Guatemala. Bull. Volcanol. 70, 1043–1067. https://doi.org/10.1007/s00445-007-0187-5.

Sears, T.M., Thomas, G.E., Carboni, E., Smith, A.J.A., Grainger, R.G., 2013. SO_2 as a possible proxy for volcanic ash in aviation hazard avoidance. J. Geophys. Res. Atmos., 118 https://doi.org/10.1002/jgrd.50505.

Sigmarsson, O., Haddadi, B., Carn, S., Moune, S., Gudnason, J., Yang, K., Clarisse, L., 2013. The sulfur budget of the 2011 Grímsvötn eruption, Iceland. Geophys. Res. Lett. 40 (23), 6095–6100.

Sisson, T.W., Layne, G.D., 1993. H_2O in basalt and basaltic andesite glass inclusions from four subduction-related volcanoes. Earth Planet. Sci. Lett. 117 (3–4), 619–635.

Stein, A.F., Draxler, R.R., Rolph, G.D., Stunder, B.J.B., Cohen, M.D., Ngan, F., 2015. NOAA's HYSPLIT Atmospheric Transport and Dispersion Modeling System, BAMS December 2015. , pp. 2059–2077 https://doi.org/10.1175/BAMS-D-14-00110.1.

Textor, C., Graf, H.-F., Herzog, M., Oberhuber, J.M., 2003. Injection of gases into the stratosphere by explosive volcanic eruptions. J. Geophys. Res. Atmos. 108, 4606. https://doi.org/10.1029/2002JD002987.

Theys, N., Campion, R., Clarisse, L., van Gent, J., Dils, B., Corradini, S., Merucci, L., Coheur, P.F., Van Roozendael, M., Hurtmans, D., Clerbaux, C., Tait, S., Ferrucci, F., 2013. Volcanic SO_2 fluxes derived from satellite data: a survey using OMI, GOME-2, IASI and MODIS. Atmos. Chem. Phys. 13, 5945–5968.

Theys, N., De Smedt, I., Yu, H., Danckaert, T., van Gent, J., Hörmann, C., Wagner, T., Hedelt, P., Bauer, H., Romahn, F., Pedergnana, M., Loyola, D., Van Roozendael, M., 2017. Sulfur dioxide retrievals from TROPOMI onboard Sentinel-5 Precursor: algorithm theoretical basis. Atmos. Meas. Tech. 10, 119–153. https://doi.org/10.5194/amt-10-119-2017.

VAAC, Volcanic Ash Advisory, 2018. National Environmental Satellite, Data, and Information Service. 4 June 2018. http://www.ssd.noaa.gov/VAAC/ARCH18/FUEG/2018F031922.html, Accessed date: 19 September 2018.

Waite, G.P., Nadeau, P.A., Lyons, J.J., 2013. Variability in eruption style and associated very long period events at Fuego volcano, Guatemala. J. Geophys. Res. Solid Earth 118 (4), 1526–1533.

Wallace, P.J., 2001. Volcanic SO_2 emissions and the abundance and distribution of exsolved gas in magma bodies. J. Volcanol. Geotherm. Res. 108, 85–106.

Webley, P.W., Wooster, M.J., Strauch, W., Saballos, J.A., Dill, K., Stephenson, P., Stephenson, J., Escobar Wolf, R., Matias, O., 2008. Experiences from near-real-time satellite-based volcano monitoring in Central America: case studies at Fuego, Guatemala. Int. J. Remote Sens. 29 (22), 6621–6646.

Whittington, A.G., Magaldi, T., Calderas, A., Chigna, G., Escobar-Wolf, R.P., Lyons, J.J., Mathias, O., Robert, G., Seaman, S.J., 2013. Magma rheology and eruption style at Volcán Fuego, Guatemala. AGU Fall Meeting Abstracts.

Witham, C., 2005. Volcanic disasters and incidents: a new database. J. Volcanol. Geotherm. Res. 148 (3–4), 191–233. https://doi.org/10.1016/j.jvolgeores.2005.04.017.

Woods, A., 1993. Moist convection and the injection of volcanic ash into the atmosphere. J. Geophys. Res. 981, 627–636. https://doi.org/10.1029/93JB00718.